Applied Catalysis B: Environmental 196 (2016) 27–40

Contents lists available at ScienceDirect

Applied Catalysis B: Environmental

journal homepage: www.elsevier.com/locate/apcatb

The effect of gold shape and size on the properties and visible light-induced photoactivity of Au-TiO_2

Anna Gołąbiewska[a,*], Anna Malankowska[d], Marcin Jarek[b], Wojciech Lisowski[c], Grzegorz Nowaczyk[b], Stefan Jurga[b], Adriana Zaleska-Medynska[a,d]

[a] Department of Chemical Technology, Gdansk University of Technology, 80-233 Gdansk, Poland
[b] NanoBioMedical Center, Adam Mickiewicz University, 61-614 Poznan, Poland
[c] Institute of Physical Chemistry, Polish Academy of Sciences, 44-52 Kasprzaka Str., 01-224 Warsaw, Poland
[d] Department of Environmental Technology, Faculty of Chemistry, University of Gdansk, Wita Stwosza 63, 80-308 Gdansk, Poland

ARTICLE INFO

Article history:
Received 10 March 2016
Received in revised form 6 May 2016
Accepted 8 May 2016
Available online 10 May 2016

Keywords:
Au-TiO2
Shap
Size
Gold NPs
Photocatalysis

ABSTRACT

In the present investigation, TiO_2 modified with a different geometry and size of gold particles, such as nanospheres (NSPs), nanostars (NSTs) and nanorods (NRs), were prepared by the immobilization method. The effect of the gold shape, size and TiO_2 matrix type (TiO_2 microspheres or rutile TIO-6_TiO_2) were systematically investigated. The obtained photocatalysts were thoroughly characterized by UV–vis diffuse-reflectance spectroscopy (DRS), BET surface area measurements, scanning electron microscopy (SEM), scanning transmission microscopy (TEM), X-ray diffraction analysis (XRD), and X-ray photoelectron spectroscopy (XPS). The photocatalytic activity under visible light ($\lambda > 420$ nm) has been estimated in phenol degradation reaction in an aqueous phase. The significantly high photocatalytic activity under visible light irradiate as demonstrated by the TiO_2 sample modified by spheres of gold. The average rate of phenol decomposition was 1.9 μmol dm^{-3} min^{-1} and was three-times higher compared to the pristine TiO_2 amorphous microspheres. On the other hand the photocatalytic activity was relatively lower and was 0.38 and 0.27 μmol dm^{-3} min^{-1} for nanorods and nanostars deposited on the amorphous form of TiO_2 microspheres, respectively. The visible light activity decreased in following order: (NSPs)> (NRs)> (NSTs). The obtained photocatalytic efficiency of samples was ascribed to the geometry and the size effect of the enhanced and the possible mechanism for this was discussed in detail. Furthermore, in this work we show the effect of calcination temperature on the structure of gold NPs, NRs and NSs before and after modification on the morphology and photocatalytic activity of Au-TiO_2.

1. Introduction

The noble metal nanoparticles (NPs) have been extensively studied for an application in areas such as spectroscopy [1–3], catalysis [4–6], photocatalysis [7–9], energy [10–12], biology [13–16] and biomedicine [17–19]. Gold particles are of a broad interest due to their unique optical properties [20,21]. The gold nanoparticles interaction with an electromagnetic radiation resulted in the free electrons oscillation in response to the electric field component. At a specific wavelength (frequency) of light, collective oscillation of electrons on the gold nanoparticle surface cause a phenomenon called localized surface plasmon resonance (LSPR) resulting in strong extinction of light (absorption and scattering). The optical properties of gold particles are strongly affected by the size and mainly by the geometry [22]. Recently, many different shapes, such as nanospheres [23], nanorods [24], nanowires [25], octahedral NPs [26], cubes NPs [20], branched crystal nanogold [27], nanostars [28] and nanotriangle [29] have been identified to be of a special interest in relation on their optical properties. Under resonant excitation, Au nanocrystals have the unique ability to concentrate the free-space optical field within subwavelength regions adjacent to their surfaces [30]. In this context the gold nanoparticles, exhibiting plasmonic properties, may activate wide band gap semiconductors, such as TiO_2, under visible light irradiation [31]. Kowalska et al. [32] investigated photocatalytic properties and influence of gold size and shape on visible-light-inducted activity. They suggested that the spherical/hemispherical shape of gold NPs in comparison with rod-like ones is beneficial for a higher level of photoactivity

* Corresponding author.
E-mail address: annagolabiewska@gmail.com (A. Gołąbiewska).

http://dx.doi.org/10.1016/j.apcatb.2016.05.013
0926-3373/

under visible light irradiation. They also observed that the wide size/shape distribution of gold NPs and thus ability of absorption of light in a broad wavelengths range are responsible for the high level of photoactivity. Liu et al. [33] reported that the TiO_2 modified by Au-nanorods exhibited high activity in an oxidation process of 2-propanol under the wide range of visible irradiation resulting from the longitudinal and transversal plasmon. Nishijima et al. [34] stated that the NRs on the surface of TiO_2 single crystal have a larger optical field and effective generation of LSPs and, consequently, can be used in a highly efficient photoelectric conversion system. They suggested that the intense optical near-field locally increased by plasmonic enhancement effects obtained due to the spatial and temporal confinement at the edge of AuNRs (especially the AuNRs/TiO_2 interface in this case) may assist the electron excitation of gold even with near-infrared wavelengths as a result of the successful electron transfer from Au NRs to the conduction band of TiO_2. Tanabe et al. [35] investigated the effect of the Au nanospheres size on the photocatalytic activities of TiO_2. It was found out that the smaller Au nanoparticles induce a larger electronic state changes a hence high photocatalytic activity in degradation process under UV light (300–400 nm) of methylene blue. Additionally, the authors observed that the gold shape had a slight effect on the electronic states of the TiO_2. Kaur et al. [36] compared co-catalytic activity of various Au nanostructures (nanorods and nanospheres) deposited on TiO_2 surface-commercially available P-25, as well as, the size effect of the obtained spheres on the photocatalytic activity. The Au-TiO_2 showed a higher photocatalytic activity in oxidation of salicylic acid under the UV light than the pure TiO_2. The highest activity was observed for TiO_2 loaded with spherical Au nanoparticles. Moreover, it was found out that the TiO_2 modified by the smallest spherical Au shows the highest catalytic activity compared to the TiO_2 modified by large spheres. Pap et al. [37] investigated the correlation between different geometries of nano-gold (spheres, triangles and wires) deposited on the surface of the commercial TiO_2 and physical properties on the photocatalytic activity of the obtained Au-TiO_2. They observed that all gold-shape loaded on TiO_2 performed the better photocatalytic activity of oxalic acid under the UV light irradiation compared to commercial P-25. Thus, according to the literature data, only few papers [35–38] deal with photocatalytic properties of TiO_2 loaded with the gold nanoparticles differing in shape, however, the effect of gold particles shape on visible light induced photocatalytic activity of Au-TiO_2 is still unclear.

In this context, TiO_2 decorated by the different shape of gold nanostructure, such as nanostars (NSTs), nanospheres (NSPs) and nanorods (NRs), were recently obtained. In this paper we show both the effect of the gold particles shape and size and TiO_2 matrix type (amorphous TiO_2 microspheres, anatase TiO_2 microspheres and rutile TIO-6 TiO_2) on the optical properties as well as visible light induced photocatalytic activity of Au-TiO_2 composites. TiO_2 microspheres were chosen due to their low density, high surface-to-volume ratio, high surface area, good surface permeability and adsorption capacities resulting in high photocatalytic activities [39–42]. It is speculated that pores in the mesoporous structured sample benefit from the penetration of vis light [43]. For the first time, the correlation between the photoactivity under visible irradiation and shape of gold nanoparticles deposited on the TiO_2 has been systematically studied. Furthermore, the effect of the application of thermal treatment step (before or after the gold nanoparticles deposition a TiO_2 microspheres) on the morphology and photocatalytic activity of the TiO_2-Au nanostars (NSTs-TiO_2), TiO_2-Au nanospheres (NSPs-TiO_2) and TiO_2-Au nanorods (NRs-TiO_2) has been investigated. The role of the different size and geometry of gold deposited on various titania matrix and the possible mechanistic aspects have also been discussed in this paper.

2. Experimental

2.1. Materials and instrument

Gold(III) chloride trihydrate ($HAuCl_4 \times 3H_2O$) and titanium(IV) n-butoxide (TBT) (>99%) from Alfa Aesar was used as gold and TiO_2 precursor in the preparation procedure. Commercial titania photocatalyst, TIO-6 (Supplier CSJ, Catalysis Society of Japan), was used as the titania source. Sodium borohydrate (98%, $NaBH_4$), silver nitrate (≥99%, $AgNO_3$), Cetyltrimethylammonium bromide (99%, CTAB), L-ascorbic acid (≥98%, AA), tannic acid ($C_{76}H_{52}O_{46}$), potassium chloride (99%, KCl) were purchased from Sigma Aldrich. Deionized water was used in all the experiments. All glassware was washed with an aqua regia (3:1 hydrochloric acid to nitric acid by volume) and rinsed copiously with water.

The surface area of the samples were evaluated from the adsorption-desorption isotherms of liquid nitrogen (77 K) detected using a Micrimeritics Gemini V (model 2365). A photocatalysts samples were dried and degassed in a sample cell at 200 °C for at last 2 h before the adsorption. The specific surface areas of the photocatalysts were determined by Brunauer-Emmett-Teller (BET) method. Powder X-ray diffraction (XRD) studies of photocatalysts samples were carried out on a Empyrean (PANalytical) diffractometer using Cu Kα radiation (1.54 Å), reflection-transmission spinner (sample stage) and PIXcel 3D detector, operating in the Bragg–Brentano geometry. The 2 Theta scans were recorded at the room temperature (300 K) in the angles ranging from 5 to 90 (°2Theta) with a step size of 0.013 (°2Th.) and continued scan mode. The XRD estimation of the crystallite size was based on the Scherrer formula: $D = 0.89\lambda/(Be - Bt)\cos\theta$, where λ is the X-ray wavelength, Be indicates the measured breadth of the peak profile, while Bt is the ideal, non broadened breadth of a peak and θ is the diffraction angle. The value of Bt was estimated on the basis of the measurements performed for a standard sample of polycrystalline Si with large crystalline grains. The X-ray photoelectron spectroscopic (XPS) measurements were performed using the PHI 5000 VersaProbe (ULVAC-PHI) spectrometer with monochromatic Al Kα radiation ($h\nu = 1486.6$ eV) from an X-ray source operating at the 100 μm spot size, 25 W and 15 kV. The high-resolution (HR) XPS spectra were collected with the hemispherical analyzer at the pass energy of 23.5 eV and the energy step size of 0.1 eV. The CasaXPS software (version 2.3.16) was used to evaluate the XPS data. The deconvolution of all HR XPS spectra, except Au 4f, was performed using a Shirley background and a Gaussian peak shape with 30% Lorentzian character. However the best fitting of Au 4f spectra was performed with the 80% Lorentzian character of the Gaussian peak shape. The binding energy (BE) scale of all detected spectra was calibrated by centering the peak $Ti2p_{3/2}$ of TiO_2 supported with BE values equal to 459.0 eV.

The morphology and distribution size of the TiO_2 nanocomposites were observed using SEM Jeol 7001TTLS microscope operated at 12 kV and Cs-corrected STEM (High Angle Annular DarkField, HAADF). The diffuse reflectance UV–vis absorption spectra of the samples was obtained using a spectrophotometer UV–VIS Double Beam, UVD-3500, Labomed, Inc. equipped with an integrating sphere where the baseline was recorded using a bare titania powders.

3. Preparation of the Au-TiO_2 nanocomposites

3.1. Synthesis of gold nanoparticles (Au NPs)

The gold nanoparticles in the shape of spheres, stars and rods, dispersed in aqueous solution, were prepared by the reduction

based method reported by Aromal et al. [44], Kozanoglu et al. [45] and Nikoobakht et al. [46], respectively.

3.1.1. Au nanospheres

The nanospheres were prepared by adding water solution of 5 ml of an tannic acid to the boiling solution of 1.3×10^{-4} M $HAuCl_4 \times 3H_2O$ and the boiling process continued for 2 min. The reduction was found out to be as fast as indicated by the red color and the reaction was completed within 1 min. The tannic acid was used as a reducing and stabilizing agent.

3.1.2. Au nanostars

(a) *Seed Solution* was prepared by the reduction of gold ions by tannic acid as described in the section 2a.

(b) *Growth of Nanorods.* The first 0.1 M CTAB solution was prepared by heating the mixture until it become clear. Then, an aqueous 0.01 M solution of the gold precursor was added to 0.1 M CTAB solution in a scintillation vial. The solution was gently mixed. In the next step, 30 μl of a 0.01 M $AgNO_3$ solution and 32 μl of a 0.1 M AA solution were added in this order. The solution was stirred on a bench top vortex mixer. Finally, 20 μl of seed solution Au NPs were added and mixing was continued for 20 s, and the solution was left undisturbed for 1 day. The color of the nanorods solution became blue–purple indicating the formation of Au nanostars. The temperature of the growth medium was kept constant at 28–30 °C in all the experiments. The reaction products were isolated by centrifugation (four times at 10000 rpm, 15 min) followed by removal of the supernatant. The precipitates were re-dispersed in a small amount of water.

3.1.3. Au nanorods

The two-step procedure was used to synthesize Au NPs nanorods:

(i) Seed Solution. 0.2 M CTAB solution was prepared by heating the sealed mixture and was mixed with 0.5 mM $HAuCl_4$ aqueous solution. Then, to the stirred solution, 0.6 ml of ice-cold 0.01 M $NaBH_4$ was added. Vigorous stirring of the solution was continued for 3 min after which the solution was kept at 27 °C for 6 h .

(ii) Growth of Nanorods. In a typical synthesis, 5 ml CTAB was added to 40 mM $AgNO_3$ solution. Then, 5.0 ml of 1 mM $HAuCl_4$ was added, followed by the addition of 70 μL of 0.0788 M L-ascorbic acid and then the solution turned from dark yellow to clear. The final step was the addition of 12 μl of the seed solution to the growth solution at 27–30 °C. After 30 s, the stirring was stopped and the mixture was left undisturbed at 28 °C for at least 30 h. The color of the solution gradually changed within 10–20 min. The reaction products were isolated by the centrifugation (four times at 1300 rpm for 20 min, 31 °C) followed by removal of the supernatant.

3.2. Preparation of TiO_2 microspheres by hydrolysis method

The TiO_2 solid spheres were prepared through controlling the TBT hydrolysis rate in ethanol. Firstly, 6 ml of TBT was diluted with ethanol in specific volume ratio. Then this solution was slowly dropped in a mixture of 96 ml of ethanol and 0.48 ml of KCl aqueous solution. After being stirred for 1 h, the suspension was left in the room temperature for 24 h. Then the precursors were washed with weather/ethanol several times and finally dried at 60 °C for 24 h. The part of the obtained powder was calcined at 400 °C for 3 h (heating rate 2 °C/min).

3.3. Preparation of Au NPs modified TiO_2

0.7 g of different titania matrix, such as TiO_2 particles (calcined or un-calcined) and TIO6_TiO_2, were dispersed in 5 ml of ethanol with the aid of ultrasonication for 10 min. Au-TiO_2 was prepared by adding a defined volume of colloidal Au NPs (stars, rods and spheres) to TiO_2 aqueous suspension followed by stirring for 24 h. The final products were dried at 50 °C for 20 h. The concentrations of gold in TiO_2 surface were 0.14 wt.% and 0.7 wt.%, respectively and were calculated based on ICP-MS method. The series with samples labeling Au_{5x}_NSPs_anatase, Au_{5x}_NRs_anatase, Au_{5x}_NSTs_anatase had a five time higher concentration (0.7 wt.%) of gold compared

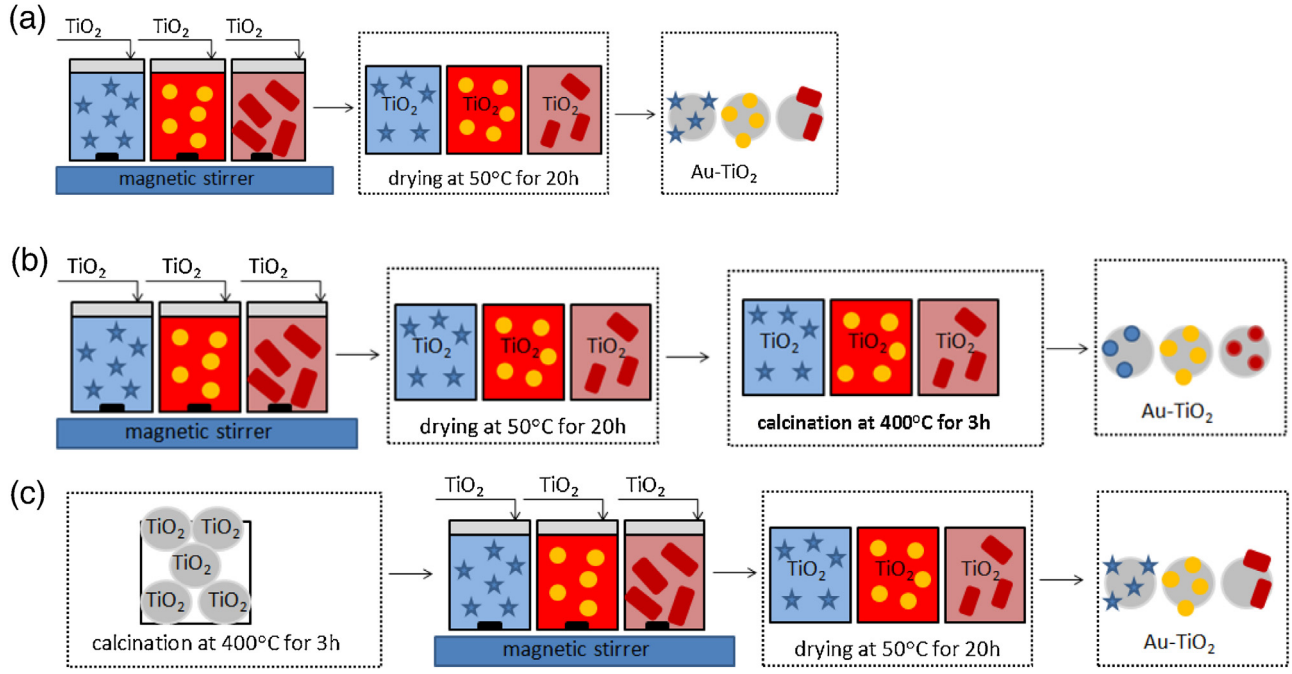

Fig. 1. Preparation routes used to obtain: (a) amorphous form of TiO_2 microspheres or rutile TiO_2 decorated with differently shaped gold nanoparticles; (b) TiO_2 microspheres decorated with differently shaped gold nanoparticles followed by thermal treatment step (calcinated after modification); and (c) calcinated TiO_2 microspheres decorated with differently shaped gold nanoparticles (calcinated before modification).

to other samples. The preparation routes of the Au-TiO_2 series are shown in Fig. 1.

3.4. Measurement of photocatalytic activity

The photocatalytic activity of Au-TiO_2 nanocomposites under visible light irradiation was investigated by measuring the decomposition rate of phenol in an aqueous solution. The photocatalysts (0.125 g) were dispersed in 25 ml of phenol solution at concentration of 0.21 mmol/dm^3 in a cylindrical reactor with a quartz window. The mixture was stirred with a magnetic stirrer and aerated (5 dm^3/h) prior to and during the photocatalytic process. Photoirradiation employed a 1000 W Xenon lamp (6271H, Oriel), which Vis light. Light passed through GG 420 filter to cut-off wavelengths shorter than 420 nm. Aliquots of 1 cm^3 of the aqueous suspension were withdrawn from the reactor at regular time periods during the illumination and filtered through a 0.2 μm syringe filter to remove fine particles of the photocatalyst. The phenol concentration was determined by colorimetric method (λ_{max} = 480 nm) after derivatization with diazo-*p*-nitroaniline using UV–vis spectrophotometer (Spectro UV–VIS Double Beam UVD-3500 Labomed, Inc.). Photocatalytic degradation runs were preceded by blind test in the absence of a photocatalysts or illumination. No degradation of phenol was observed in the absence of either the photocatalyst or illumination.

4. Results and discussion

4.1. Microscopy analysis

Sample labeling, preparation route and characterization of the five series of nanocomposites are given in Table 1. The morphology of TiO_2 microspheres was confirmed using scanning electron microscopy (SEM), since the shape of gold nanoparticles was observed both with scanning electron microscopy (SEM) and the transmission electron microscopy (TEM). Fig. 2 shows the morphology of gold colloids obtained by the three different strategies together with corresponding statistical size distribution of Au particles. The average Au size (dAu) was calculated from the statistical average size of 100 Au NPs. The TEM images of well-defined Au NRs with narrow size distribution of ~44 nm in length and ~16 nm in relatively large diameter (length/width aspect ratio 2.75) is shown in Fig. 2a. The major fraction of Au NRs appears with an average length size equaled to 43.8 nm. It was observed that the separation of nanorods was successfully accomplished using the described centrifugation conditions. For spherical particles dispersed in the colloidal solution the average diameter was about ~23.3 nm as shown in Fig. 2b. The nanospheres characterize the similar size and morphology with the range from 13.3 to 23.3 nm. The major fraction of Au NSPs appears with an average size and was 23.3 nm. Fractions from the range of 6–10 nm and about 26.7 nm represented a very small part in the test sample. The high-yield nature of the stars as well as their complex morphology and homogeneous distribution are presented by the SEM images in Fig. 2c. The average Au size was measured from one end to another of the branches through the nanostars center. The major fraction of Au NSTs appears with an average size equaled to 150 nm. The average branches lengths of the nanostars range between the sizes of 50–90 nm.

The distribution size of TiO_2 microspheres, used as a matrix for a different shape of nanogold is presented in Fig. 3a. The two main fractions of TiO_2 microspheres have been recognized. The dominant fraction were the smaller microspheres (⊘ ca. 333–375 nm) and the second one was significantly bigger (⊘ ca. 583–600 nm). The microscopy observation confirmed the existence of gold nanoparticles with the various geometry on the surface of TiO_2 microspheres, obtained by surface immobilization. Fig. 3b–d shows SEM images of gold nanoshape (nanorods, nanosphere and nanostars) deposited on the amorphous form of TiO_2 microspheres. The gold particles are seen as bright contrasts on the surface of TiO_2 particles. The average nanorods lengths and diameters were 44 nm and 16 nm, respectively. It was observed that the average spheres size of gold were about 23 nm. Moreover, the obtained Au NSPs were formed

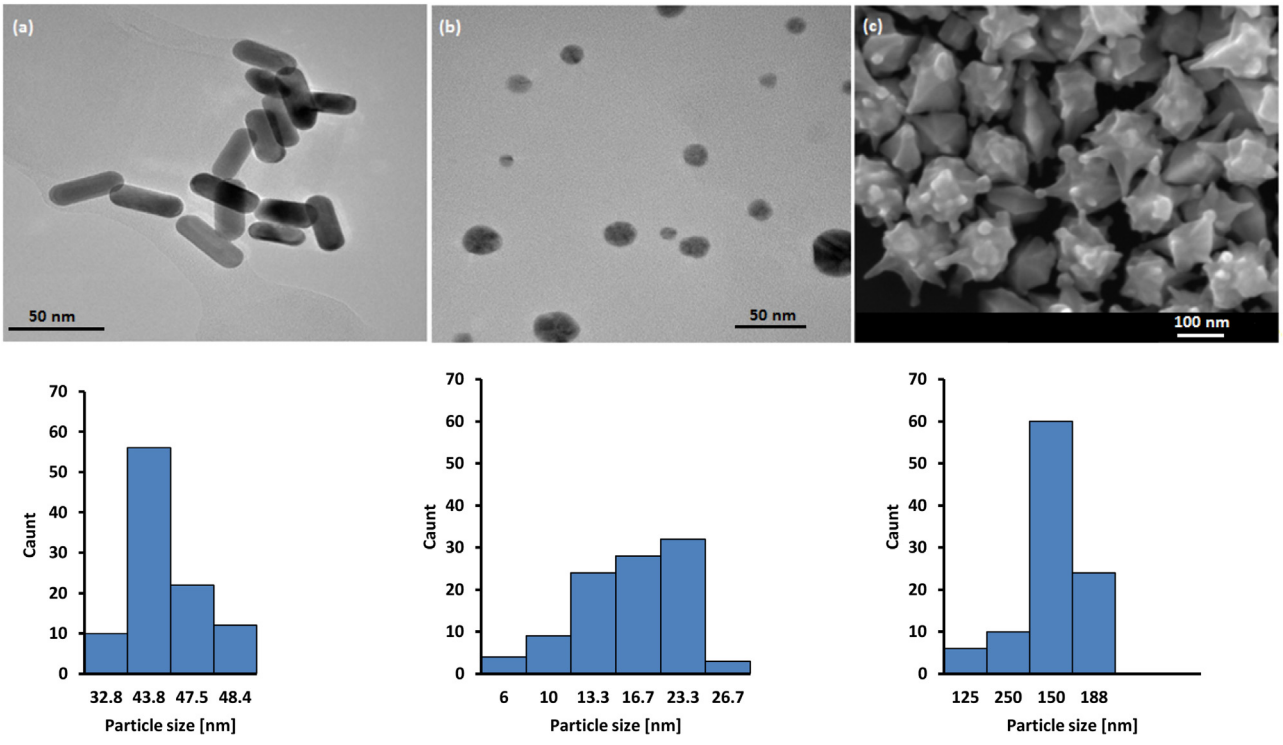

Fig. 2. Morphology (TEM/SEM images) and average size distribution of (a) gold nanorods and (b) gold nanospheres (c) SEM image of gold nanostars.

Table 1
Sample label, preparation conditions and selected properties of TiO_2 loaded with gold nanoparticles with different shapes.

Sample label	TiO_2 matrix	Shape of gold before immobilization at the surface of TiO_2 spheres	Preparation route	Shape of gold before immobilization at the surface of TiO_2 spheres	LSPR, λ_{max}	BET surface area [m^2/g]	Rate of phenol degradation under visible light ($\lambda > 420$ nm) ($\mu mol\ dm^{-3}\ min^{-1}$)
TiO_2_amorphous	TiO_2 microspheres		sol-gel without calcination	–	–	262	0.61
Au_NSPs_TiO_2	amorphous TiO_2 microspheres	spheres	Au nanoparticles deposition at amorphous TiO_2 without calcination	spherical	400	243	1.88
Au_NRs_TiO_2	amorphous TiO_2 microspheres	rods		rods	524 and 673	249	0.38
Au_NSTs_TiO_2	amorphous TiO_2 microspheres	stars		stars	557	257	0.27
TiO_2_anatase	anatase TiO_2 microspheres		sol-gel followed by calcination	–	–	46	0.43
Au_NSPs_anatase_C	anatase TiO_2 microspheres	spheres	Au nanoparticles deposition at amorphous TiO_2 followed by calcination (calcinated after modification)	spherical	554	78	0.69
Au_NRs_anatase_C	anatase TiO_2 microspheres	rods		spherical	562	63	0.57
Au_NSTs_anatase_C	anatase TiO_2 microspheres	stars		spherical	592	60	0.58
Au_NSPs_anatase	anatase TiO_2 microspheres	spheres	Au nanoparticles deposition at calcinated TiO_2 (calcinated before modification)	spherical	410	75	0.88
Au_NRs _anatase	anatase TiO_2 microspheres	rods		rods	542 and 613	67	0.31
Au_NSTs_anatase	anatase TiO_2 microspheres	stars		stars	584	65	0.26
Au_{5x}_NSPs_anatase	anatase TiO_2 microspheres	spheres	Au nanoparticles deposition at calcinated TiO_2 (calcinated before modification) concentration of gold five time higher	spherical	413	89	0.75
Au_{5x}_NRs _anatase	anatase TiO_2 microspheres	rods		rods	543 and 611	68	0.26
Au_{5x}_NSTs_anatase	anatase TiO_2 microspheres	stars		stars	662	67	0.17
TIO6_rutile	TIO6 rutile		Supplier CSJ: Catalysis Society of Japan			76	0.38
Au_NSPs_rutile	TIO6 rutile	spheres	Au nanoparticles deposition at TIO5_TiO_2 without calcination	spherical	431	78	1.17
Au_NRs_rutile	TIO6 rutile	rods		rods	535 and 654	70	1.10
Au_NSTs_rutile	TIO6 rutile	stars		stars	581	67	0.62

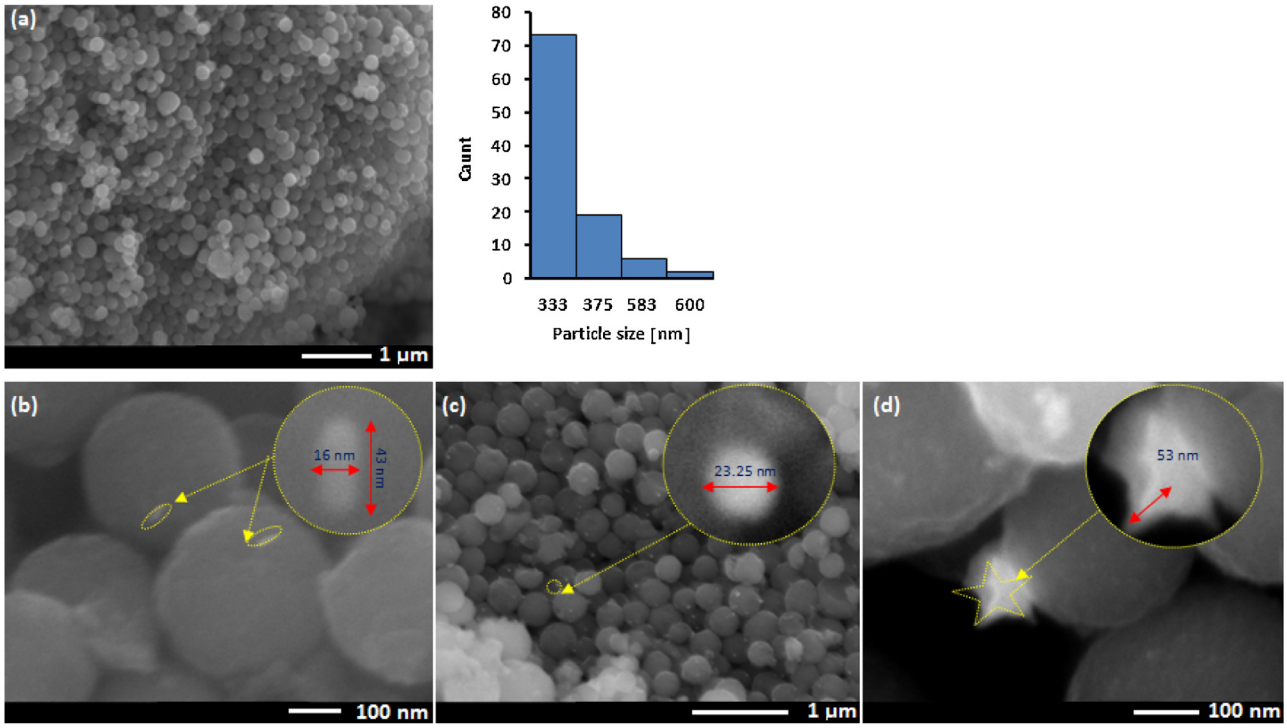

Fig. 3. Microscopic characterization of TiO_2 microspheres and Au loaded TiO_2 microspheres: (a) SEM images and average size distribution of TiO_2 microspheres; (b) SEM images of TiO_2 microspheres loaded with gold nanorods; (c) SEM images of TiO_2 microspheres loaded with gold spheres; and (d) SEM images of TiO_2 microspheres loaded with gold nanostars.

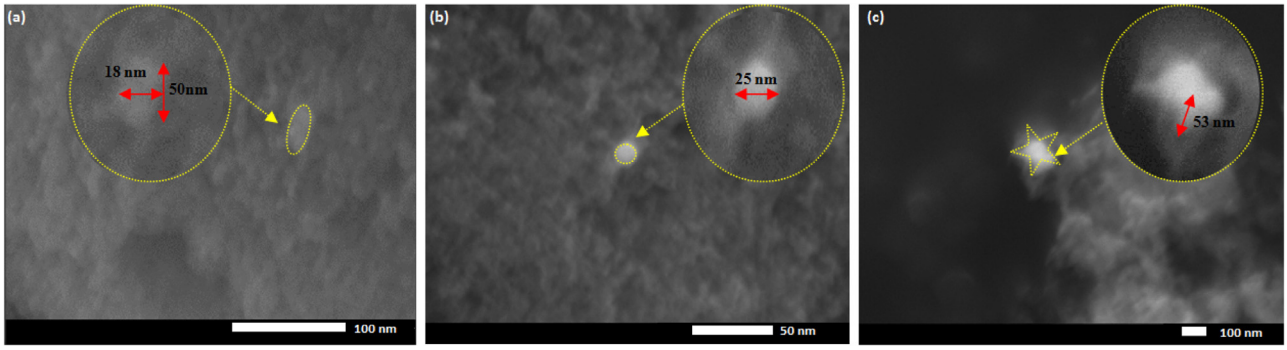

Fig. 4. SEM images of Au-TiO_2 obtained by deposition of: (a) gold nanorods, (b) gold nanospheres, and (c) gold nanostars at the surface of rutile TiO_2.

dominantly and uniformly distributed on microspheres of the TiO_2 surface. The average stars lengths branches deposited on the TiO_2 were about 53 nm.

Fig. 4a–c shows SEM image of the resulting nanostructures of gold deposited on the rutile surface. The average spheres size of gold was about 25 nm. The obtained Au NRs possess longitudinal length (ca.50 nm) and transverse length (ca.18 nm). The average stars lengths branches deposited on the rutile powders were about 53 nm. Generally, it was observed that both, the shape and the size, of the NRs, NSPs and NSTs of gold deposited on the surface of TiO_2 (rutile powder and microspheres) did not change in relation to the starting colloidal solutions discussed above.

The SEM technique was also applied to observe the Au-TiO_2 nanocomposites obtained by gold nanoshapes immobilization at the surface of amorphous TiO_2 microspheres followed by calcination at 400 °C. The microscopy analysis revealed the existence only of spherical gold of various size about ~35 nm, 50 nm and 75 nm, independently on the shape of gold nanoparticles used during preparation route (see details in Fig. 5a–c). Thus, all shapes of gold deposited on TiO_2 microspheres were deformed by thermal treatment as schematically shown in Fig. 6. It could be assumed that the nanostars branches were destroyed during the thermal treatment at 400 °C followed by melting of the nanostars centers and finally resulted in the increase of their volume and diameters. Next, the star center is in contact with deformed nanostars branches. These misshapen nanostars undergo sintering to larger clusters and creating nanospheres with an average size of 75 nm. Entirely different situation was observed for nanorods and nanospheres. The thermal treatment caused that the gold nanorods and nanospheres were melting and finally formed larger agglomerates of gold as shown in Fig. 6. This is consistent with the suggestion that the gold has a quite low surface free energy (1.626 J/m^2) [41]. Therefore, the liquid with a low surface energy (melted gold) tends to form curved surfaces in order to minimize the area. Moreover, the binding energy of Au to an oxide support is to be much smaller than the Au–Au bond. These relative energy differences lead to facile sintering of Au nanoparticles as a function of reaction time, i.e. small, highly dispersed particles eventually convert to thermody-

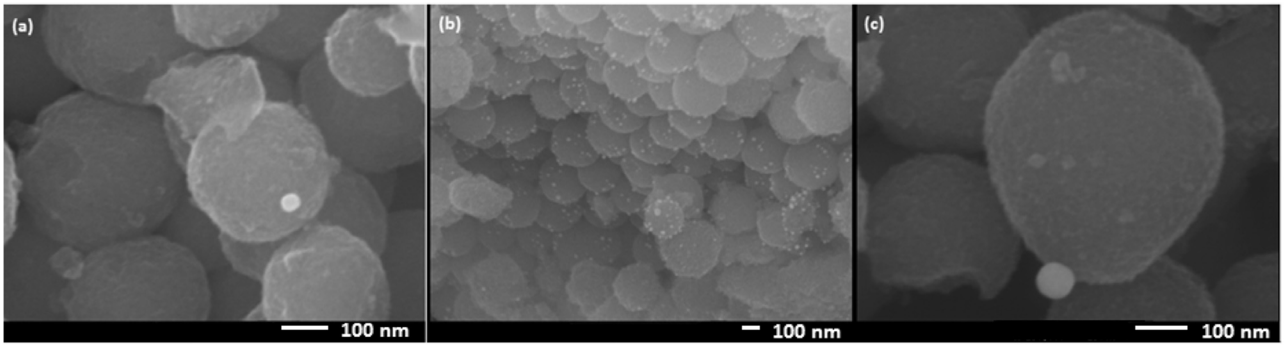

Fig. 5. SEM images of Au-TiO_2 obtained by deposition of: (a) gold nanorods, (b) gold nanospheres, and (c) gold nanostars at the surface of TiO_2 microspheres followed by calcination at 400 °C.

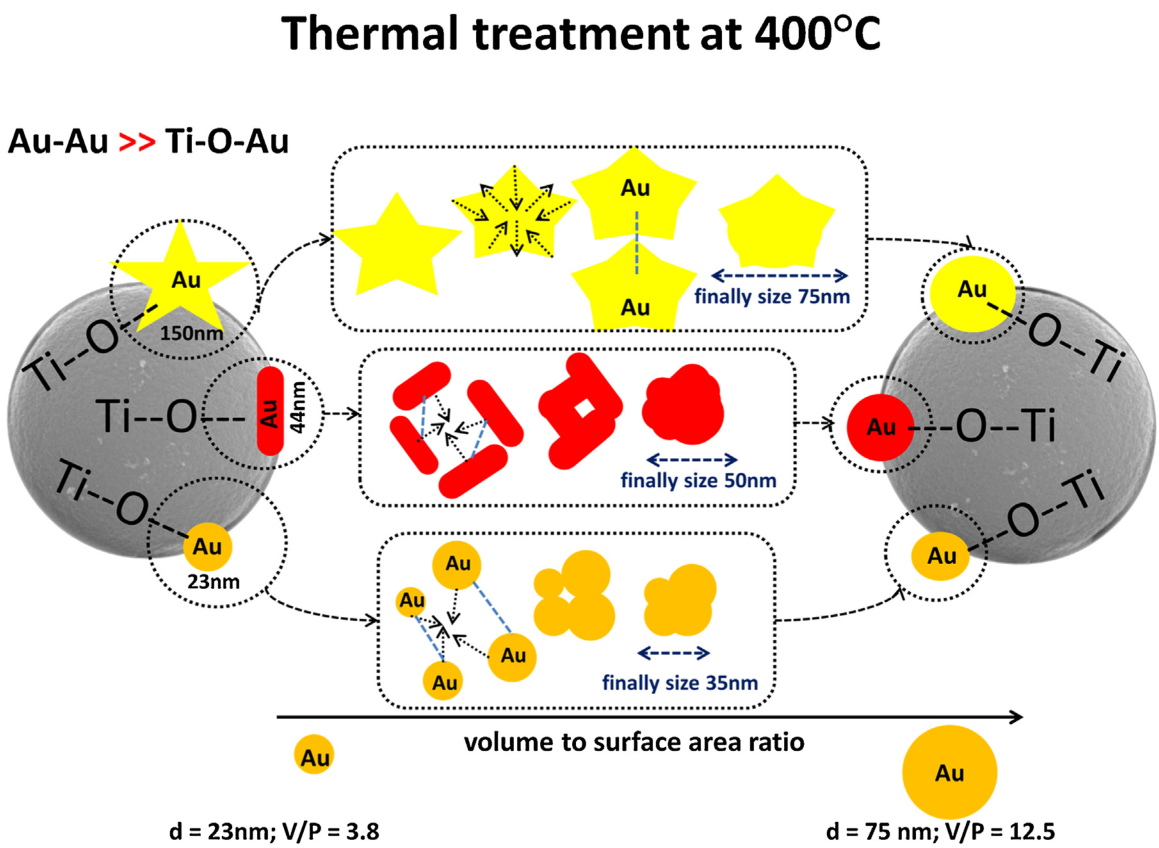

Fig. 6. Schematic mechanism of the Au gold nanoparticles transition during thermal treatment of TiO_2 microspheres loaded with gold nanostars, nanospheres and nanorods.

namically preferred larger particles [47]. The larger particles are more energetically favored due to their greater volume to surface area ratio and that is why this thermodynamically-driven process take place spontaneously [47], as shown in Fig. 6. The noticeable difference in size of gold particles before and after calcination process was clearly observed. For the samples containing gold NSPs and NRs and calcined at 400 °C, the average size of gold particles increased from 23 and 44 nm up to about 35 and 50 nm, respectively. Sintering of gold nanospheres and increase in size from 23 to 35 nm resulted in rise of volume to surface area ratio from 3.8 to 5.8, respectively. Equally in the case of gold nanorods, transformation from cylindrically shaped (⊘: 16 nm; h: 44 nm) to spherical particles (⊘: 50 nm) caused to enhancement of volume to surface area ratio from 3.9 to 8.3, respectively. Thus, the enlarge of both sizes as well as the shape transformation were thermodynamically favored.

Only in the case of gold nanostars it was observed that under high temperature (400 °C) they were melted and formed particles smaller than initial ones. The average size of gold NSTs after thermal treatment was two times lower and equaled to 75 nm. Referring to the paper of Wen et al. [48], their results indicated that the calcination temperature of 350 °C promotes the migration of Au particles through melting the smaller Au NPs. They observed that the small Au NPs at interfaces are sintered to form larger Au NPs, which reduces the joint active sites while the temperature increases from 350° to 450 °C. Akita et al. [49] revealed that with an increase in calcination temperature, Au particles grow to larger particles by cluster mobility and Ostwald ripening. They found out that the Au clusters that are trapped at defect sites of TiO_2 cannot grow so much in the temperature ranges from room temperature to 200 °C. At 200 °C Au clusters diffuse on the TiO_2 particle surface to grow to larger particles, but they cannot diffuse on the whole TiO_2

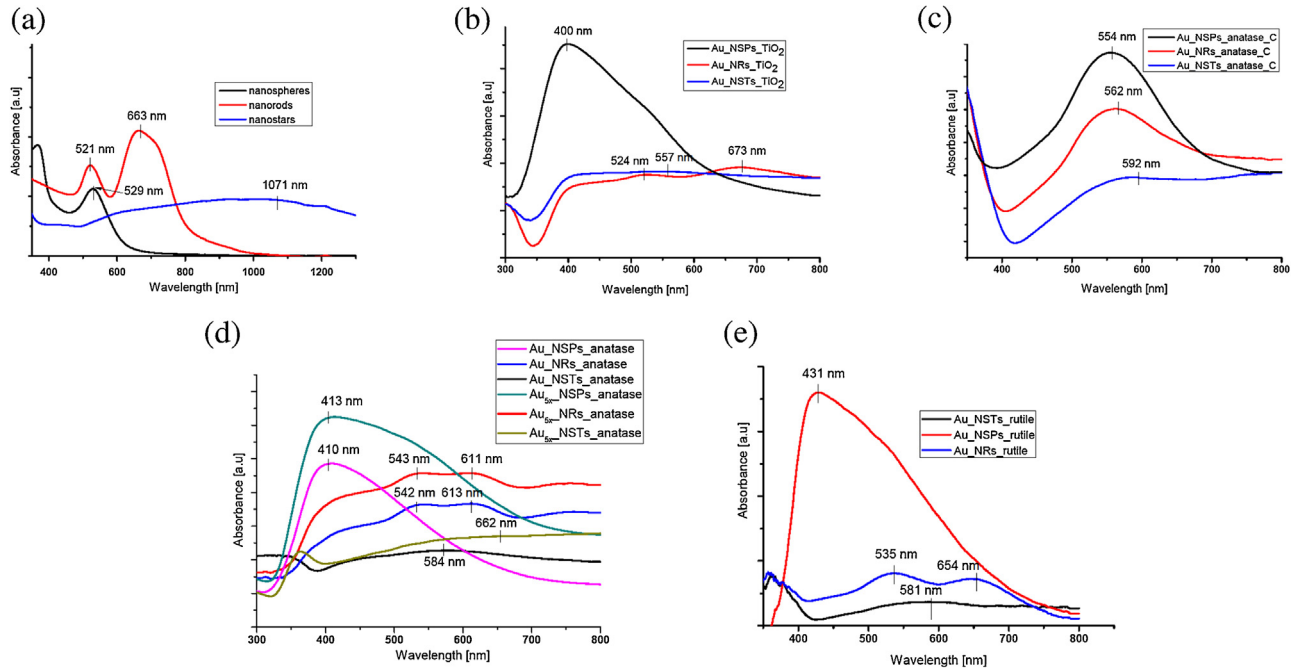

Fig. 7. UV–vis absorption spectra of: (a) differently shaped gold nanoparticles dispersed in aqueous solution; (b) differently shaped gold nanoparticles deposited at the surface of non-calcinated TiO_2 microspheres; (c) differently shaped gold nanoparticles deposited at the surface of TiO_2 microspheres and finally calcinated at 450 °C, and (d) differently shaped gold nanoparticles deposited at the surface of preliminary calcinated TiO_2 microspheres (e) differently shaped gold nanoparticles deposited at the surface of non-calcinated rutile TiO_2.

particle surface. The increase in temperature above 300 °C resulted in possibility of Au clusters and atoms mobility on the whole surface of TiO_2 particles. Each Au particle could arrive and encounter the interface between TiO_2 particles acting as sinks for au NPs [49].

4.2. Absorption properties and BET surface area

The localized surface plasmon resonance (LSPR) indicates for the optical properties of gold. Fig. 7a shows the spectra absorption of different shape of gold dispersed in the colloidal solution. The nanorods (NRs) exhibited longitudinal and transversal plasmon peak with maxima at 521 nm and 663 nm, respectively. Additionally, this presence provides the two characteristic peaks suggests that the sample was homogenous and contains mainly gold nanorods. According to the literature data, the gold nanorods with cylindrical symmetry usually exhibit two plasmon modes: (i) a longitudinal LSP mode associated with the electron oscillations along the length direction, and (ii) a transverse TSP mode arising from the transverse electron oscillations [30,50–53].

For the particles spheres (NSPs) the characteristic localized surface plasmon resonance (LSPR) band maximum is observed at 529 nm. This peak position suggests the presence of the spherical gold NPs of about ~30 nm size. Zhong et al. [54] observed one plasmon band with the maximum of small (ca. 20 ± 5 nm) hollow spherical gold at 527 nm.

One broad absorption band at about 1071 nm was observed in the case of nanostars particles (Fig. 7a). The gold nanostars are expected to display LSPRs that are red-shifted with respect to those for spheres of similar sizes, as well as very high electromagnetic fields localized at each tip [55]. Kooij et al. [56] revealed that the shape of the branches and their mutual interaction of gold nanostars determined the absorption ranges. They observed three distinct peaks at wavelengths of 575 nm and 700 nm and a strong absorption centered at around 1200 nm for the shape-controlled nanostars. The latter peak is ascribed to the plasmon resonance along the length of the branches, i.e. a longitudinal resonance and was characteristic for shapes of the well-defined nanostars. Moreover, the position of LSPR is more strictly dependent on the shape and size of the nanorods that was used as starting materials to obtained the nanostars of gold [28,57,58]. According to our observations dominant the plasmon band at longer wavelengths (1071 nm) was supported by the nanostars branches.

The UV–vis absorption spectra of the amorphous form of TiO_2 microspheres decorated with gold nanoparticles are shown in Fig. 7b. All DR spectra were taken using bare titania: TiO_2 amorphous, TiO_2 anatas, TIO6 rutile as a reference materials. The TiO_2 calcinated at 400 °C was used as a reference material for series calcinated after and before modification of gold. The rutile was used as a reference material for series of TIO6 modified with different shape of gold. The nanorods exhibited two main peaks: longitudinal (ca.673 nm) and transverse (ca.524 nm). These results were consistent with previous results discussed for nanorods dispersed in the colloidal solution. The absorption spectrum of Au nanospheres exhibits a broad, intense band centered at about 400 nm, along with a less intense shoulder at 520 nm. In the contrast of the above types only nanostars exhibited one characteristic band at about 557 nm. There has been a clear shift in LSPR peak position which may be related to the properties of titania such as surface defects, shape and uniformity.

DR spectra of nanoshape deposited at the surface microspheres TiO_2 in Fig. 7c. The obtained nanocomposites of Au-TiO_2 were calcinated at 400 °C. The only one characteristic localized surface plasmon resonance (LSPR) band maximum is observed at about 554 nm, 562 nm and 592 nm for the gold NSPs with a different size from 35 to 75 nm. Based on the SEM analysis, it was observed that the nanoshapes of gold deposited on the TiO_2 surface and then calcinated, were destroyed by heating. One peak in absorption spectra in the region of 550–600 nm could be attributed to the presence of gold NSPs. Moreover, the different positions of the LSPR suggesting that the resulting gold NSPs varying with size. It has been demonstrated that the gold NSPs of a smaller size (~25 nm and 50 nm) deposited at microspheres TiO_2 surface the LSPR peaks

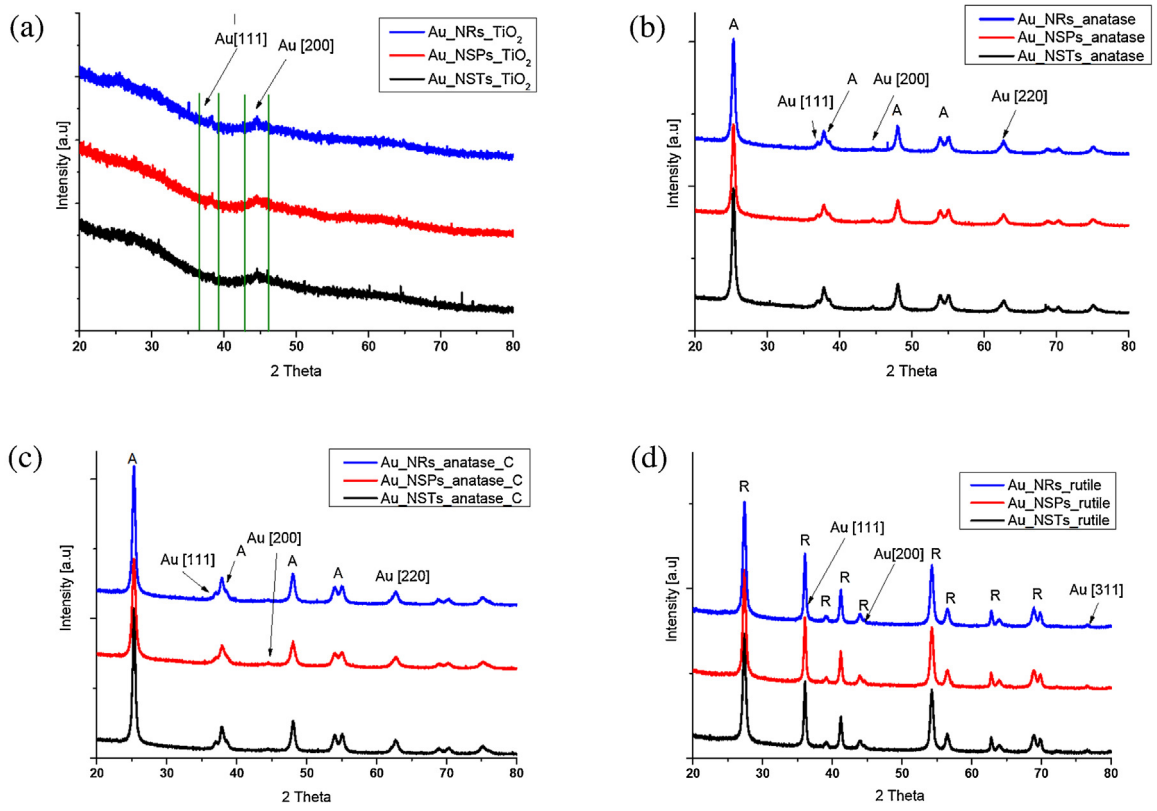

Fig. 8. X-ray diffraction pattern of: (a) differently shaped gold nanoparticles deposited at the surface of non-calcinated TiO_2 microspheres; (b) differently shaped gold nanoparticles deposited at the surface of preliminary calcinated TiO_2 microspheres (d) differently shaped gold nanoparticles deposited at the surface of TiO_2 microspheres and finally calcinated at 450 °C (e) differently shaped gold nanoparticles deposited at the surface of non-calcinated rutile TiO_2.

were observed at shorter wavelengths (550–560 nm), unlike for large particles (~75 nm) which the absorbing longer wavelength (592 nm). The UV–vis absorption spectra of anatase microspheres of TiO_2 modified by nanoshape of gold are shown in Fig. 7d. Two main peaks in their absorption spectra with the maximum at about 542 nm and 613 nm could be attributed to the presence of gold nanorods Au_NRs_anatase, while in case of the gold nanospheres Au_NSPs_anatase, absorption band at 410 nm was observed. In the case of nanostars Au_NSTs_anatase, one main LSPR peak with the maximum at 584 nm, was observed. In the series with 5 time higher concentrations of gold a prominent plasmon around 413, 542 and 613, 662 nm were observed for spheres, rods and stars, respectively. In the case of TiO_2 modified with Au nanostars it was observed significantly shift of the surface plasmon resonance to shorter wavelength probably strongly depended on the surface defect of TiO_2. However, the surface plasmon bands exhibited blue-shifts for Au nanostars and also depends on the number and length of the branches [59]. The UV–vis absorption spectra of nanoshape of Au deposited on the rutile is shown in Fig. 7e. The nanorods (NRs) possess longitudinal and transversal plasmon peak with the maximum at 535 nm and 654 nm, respectively. While, the absorption spectrum of small (ca. 25 ± 5 nm) hollow spherical gold exhibits a broad, intense band centered at about 413 nm, along with a less intense shoulder at 520 nm. In the case of spheres of gold deposition at (i) rutile TIO-6, (ii) TiO_2 microspheres without calcination and, (*iii*) anatase TiO_2 microspheres, one plasmon band was detected for much shorter wavelengths. It was suggested that the dielectric properties of the surrounding medium is also a key factor after the size and shape of gold on the position of LSPR [60]. The LSPR was affected by the refractive index of the ambient medium since the polarization of the particles will induce an opposing polarization in the ambient media. The liquid does not interact chemically with the surface but increases the refractive index, and a stepwise shift of the LSPR peak [61]. Kowalska et al. [31] stated that the absorption peaks at 320 nm and 430 nm corresponding the presence of gold particles of 2 nm in size. Moreover, they found out that the peak wavelength of LSPR might depend on the solvent and on the size and shape of titania particles [62]. In the case of nanostars, one main LSPR peak with the maximum at 581 nm, was observed.

The Au–TiO_2 samples without calcination had the highest BET surface area ranged from 242 to 256 m^2/g (see Table 1). In the case of samples calcinated after and before modification by gold it was observed that the BET surface area was reduced, due to sintering and crystal growth of TiO_2 particles [63,64]. The BET surface area was fluctuated from 65 to 75 m^2/g for the nanocomposites calcinated after modification by gold. For the preliminary calcinated TiO_2 microspheres and then modified by gold the BET surface area changed from 60 to 78 m^2/g.

The BET surface area for the Au nanoparticles deposited at rutile without calcination was fluctuated from 67 to 78 m^2/g. It was noticed that this surface area of anatase TiO_2 microspheres and rutile TIO-6 do not differ from each other. It is related with the crystallites size: the former one consisted of the average crystallites size for all the phases around 18.6–20 nm [65].

4.3. XRD analysis

The TiO_2 crystal structure and gold crystal system was evaluated using the XRD analysis (shown in Fig. 8a–d). The diffraction peaks of 38.3°, 44.2° could be attributed to gold appeared for samples of gold NRs, NSTs, NSPs deposited at amorphous TiO_2 microspheres.

The typical diffraction peaks corresponding to anatase ($2\theta = 25°$, 38°, 48°, 54°) were observed in two series of preliminary and finally calcinated at 450 °C TiO_2 microspheres. The average crystallite size

of anatase for the samples calcinated after modification of gold was calculated from the (101) plane in the XRD pattern in the range of 20.1–20.5 nm. In the case of series calcinated before modification the average size of anatase crystallites was between 15.8 and 21.3 nm. The reflections of Au [111], [200] and [220] appear at 38.3°, 44.2° and 63.8, were observed, respectively. The reflections attributed to rutile were indexed at 27.2°, 36.4°, 39°, 42.1°, 54.2°, 63° and 67.5° for the TIO-6 modified by different geometry of gold, confirming the presence of a single phase. The diffraction pattern like [111], [200] and [311] indicate the presence of gold on the rutile surface. For the all samples, the XRD data indicates that the crystal system for titania and gold (spheres, rods and stars) was tetragonal and cubic, respectively.

4.4. XPS analysis

Both pure TiO_2 and Au-modified TiO_2 samples were analyzed using XPS technique. Table 2 shows the composition and chemical characters of elements formed in the surface layer of various TiO_2 (amorphous, anatase, rutile) modified with different geometry of gold nanospecies as nanospheres (NSPs) nanostars (NSTs) and nanorods (NRs). The presented XPS data was obtained after analysis of high-resolution (HR) XPS spectra of Ti2p, O1s, C1s and Au 4f for all detected elements; titanium, oxygen, carbon and gold, respectively. Two chemical states of titanium were separated in the Ti 2p spectrum at the BE of Ti $2p_{3/2}$ peak close to 459.0 eV and 457.2–457.6 eV, which can be identified as Ti^{4+} and Ti^{3+}, respectively [64,66]. The O1s spectrum can be composed of two different peaks, at BE of 530 ± 0.1 eV and 531.3 ± 0.3 eV, which can be described as bulk (TiO_{latt}) and surface (TiO_{surf}) states of TiO_2. The last O1s state can be also accompanied by C=O surface species [67]. For some samples (see Table_2) also additional O 1s state was detected at BE of 533.4 eV, which can be assigned to —OH and C—O groups [67]. The C 1s region can be deconvoluted for three peaks, at BE of 285.0 eV, 286.5 eV and 289.3 eV, which can be attributed to C—C, C—O and C=O bounds, respectively [68]. The Au 4f spectra were fitted successfully with 2 components, which can be representative for differently charged Au nanoparticles. The metallic gold (Au^0) at BE = 83.6–84.2 eV, is a dominant form of gold species in all Au-modified samples collected in Table 2. The BE lower than 84.0 eV, found for some samples, can be interpreted as a result of interaction between metallic gold clusters and the surface Ti^{3+} centers at defects in the titania [69,70]. The electropositive ($Au^{\delta+}$) state, at BE > 85.0 eV, can be related to highly dispersed gold clusters deposited at the surface of titania. Such highly dispersed gold nanoparticles of size ≤12–14 nm were found to shift the BE by +0.3 eV with respect to the BE of core-electrons in the bulk gold [71].

Inspection of XPS data, collected in Table 2 revealed the total surface content of gold (0.6–5.2 wt.%) in all Au-TiO_2 nanocomposites to be much larger than the bulk concentration determined by preparation procedures (0.14 wt.%). That clearly evidences the surface aggregation of Au species as a result of preparation procedures. The relative carbon and gold surface concentrations were found to be the largest for NSPs and much smaller for NRs and NSTs nanocomposites at all types of TiO_2 supports (amorphous, anatase and rutile). From the other hand, one can observe the electropositively charged Au species, characteristic for the highly dispersed gold clusters, to be the most pronounced in NSTs and less contributed in NRs and NSPs (see Table 2). This tendency is observed in both anatase and rutile supported samples.

The effect of preparation route can be analyzed for anatase supported samples. In Fig. S1 the HR spectra of C 1s and Au 4f are presented for the TiO_2–anatase samples, calcinated before and after modification by NSTs, NRs and NSPs Au species. The samples calcinated before modification exhibit much larger content of carbon

Table 2
Elemental composition (in wt.%) and chemical characters of Ti, O, C and Au states in the surface layer of TiO_2 modified with a different geometry of gold such as nanospheres (NSPs). nanostars (NSTs) and nanorods (NRs) evaluated by XPS analysis.

Sample label	$\sum$ Ti (wt.%)	Fraction Ti state (%)		$\sum$ O (wt.%)	Fraction O state (%)			$\sum$ C (wt.%)	Fraction C state (%)			$\sum$ Au (wt.%)	Fraction Au state (%)	
		Ti 4 + 459.0 eV	Ti 3+ 457.2–457.6 eV		$Ti\text{-}O_{latt}$ 530.3 ± 0.1 eV	$Ti\text{-}O_{surf}$, C=O 531.3 ± 0.3 eV)	—OH, C—O 533.4 eV		C—C 285.0 eV	C—O 286.5 eV	C=O 289.3 eV		Au^0 83.6–84.2 eV	$Au^{\delta+}$ > 85.0 eV
TiO_2_amorphous	50.0	85.5	15.5	40.2	55.3	44.7	–	9.8	63.9	34.5	1.6	–	–	–
Au_NSPs_TiO_2	26.8	98.0	2.0	43.0	25.5	41.2	33.3	28.7	40.6	49.8	9.6	1.5	60.0	40.0
Au_NRs_TiO_2	50.5	89.9	10.1	40.2	69.0	31.0	–	6.4	64.2	28.2	7.6	2.9	93.5	6.5
Au_NSTs_TiO_2	51.9	85.3	14.7	40.3	68.2	31.8	–	7.1	64.2	30.5	5.3	0.7	81.9	18.1
TiO_2_anatase	54.7	95.8	4.2	41.1	79.4	20.6	–	4.2	65.6	29.1	5.3	–	–	–
Au_NSPs_anatase_C	52.6	94.3	5.7	39.8	79.6	20.4	–	5.5	64.0	30.8	5.2	2.1	95.2	4.8
Au_NRs_anatase_C	53.9	93.4	6.6	40.9	78.6	21.4	–	4.2	66.8	28.3	4.9	1.0	91.0	9.0
Au_NSTs_anatase_C	53.6	96.0	4.0	41.1	83.8	16.2	–	4.7	69.3	18.9	11.8	0.6	76.6	23.4
Au_NSPs_anatase	28.5	97.5	2.5	40.9	37.9	27.5	34.6	25.4	47.0	45.0	8.0	5.2	97.3	2.7
Au_NRs_anatase	51.7	95.2	4.8	38.8	81.0	19.0	–	7.2	77.1	16.9	6.0	2.3	94.6	5.4
Au_NSTs_anatase	52.9	96.0	4.0	40.7	82.5	17.5	–	5.6	74.3	17.3	8.4	0.8	78.0	22.0
TIO6_rutile	53.0	92.7	7.3	42.8	75.2	24.8	–	4.2	64.3	27.7	8.0	–	–	–
Au_NSPs_rutile	45.9	97.2	2.8	42.7	65.4	24.6	10.0	10.2	44.5	46.4	9.1	1.2	89.0	11.0
Au_NRs_rutile	53.0	92.1	7.9	42.3	76.1	23.9	–	3.9	66.1	26.5	7.4	0.8	67.1	32.9
(Au_NSTs_rutile	51.7	94.7	5.3	42.1	79.0	21.0	–	5.5	69.8	14.3	15.9	0.7	65.8	34.2

Table 3
The quantity (mg) of gold per gram of TiO_2 evaluated by ICP-MS analysis.

Sample label	The quantity (mg) of gold per gram of TiO_2
Au_NSPs_anatase	0.33
Au_NRs _anatase	0.19
Au_NSTs_anatase	0.25
Au_{5x}_NSPs_anatase	2.6
Au_{5x}_NRs _anatase	1.1
Au_{5x}_NSTs_anatase	0.3
Au_NSPs_rutile	0.1
Au_NRs_rutile	0.28
Au_NSTs_rutile	0.35

and gold surface species than the corresponding samples calcinated after modification (see also Table 2). We can observe also a different distribution of the fraction states of carbon and gold. The TiO_2 sample, calcinated prior to modification by Au NSPs, is covered by larger amount of carbon-oxide compounds than the sample calcinated after modification (Table 2 and Fig. S1 in Supporting materials). The large amount of C—O surface species on this sample is also reflected by oxygen O1s peak at BE = 533.4 eV (Table 2). Moreover, the Au nanoparticles deposited at calcinated TiO_2 exhibit relative smaller contribution of the $Au^{\delta+}$ gold species than Au nanoparticles deposited at amorphous anatase samples.

Additionally, the amount of gold incorporated into TiO_2 was verified by ICP-MS measurements and equaled form 0.1–2.6 mg per gram of TiO_2 as show in Table 3. It was observed that the increase in the amount of gold colloid used during the preparation caused an increase in the amount of gold on the surface of TiO_2 microspheres for gold in the form of spheres and rods. However, it wasn't observed an increase in the amount of adsorbed/immobilized nanostars.

4.5. Photocatalytic activity under visible light

The photocatalytic activity of as-prepared samples was evaluated using aqueous solution of phenol as a model pollutant. The photocatalytic efficiency of TiO_2 decorated with different shape of gold particles, such as nanorods, nanospheres and nanostars samples, are shown in Table 1. The obtained results indicated that the photocatalytic activity under visible light depends on the geometry and size of gold nanoparticles used for TiO_2 modification. Generally, it could be concluded that the sphere-shaped gold particles decorated TiO_2 possess the highest visible light induced activity among all Au-TiO_2 samples. The rate of phenol degradation equaled to 1.88, 0.69, 0.88 and 1.17 $\mu mol\,dm^{-3}\,min^{-1}$ for NSPs-decorated amorphous TiO_2 microspheres, anatase microspheres calcined after modification, anatase microspheres calcined before modification and rutile, respectively. The highest photocatalytic activity under visible light irradiation was demonstrated by amorphous TiO_2 microspheres modified by spherical gold particles. The average rate of phenol decomposition was 1.88 $\mu mol\,dm^{-3}\,min^{-1}$ and was three-times higher compared to pure microspheres TiO_2 (0.61 $\mu mol\,dm^{-3}\,min^{-1}$). On the other hand the photocatalytic activity was relatively lower and equaled to 0.38 and 0.27 $\mu mol\,dm^{-3}\,min^{-1}$ for nanorods and nanostars deposited on microspheres of TiO_2, respectively. From the XPS analysis, it was observed that the surface defect (Ti^{3+}) was successfully created on the amorphous form of TiO_2 ($Ti^{3+} \sim 15.5\%$). The highest surface area of this sample (262 m^2/g) associated with the presence of the a large amount of Ti^{3+} active sites. The Ti^{3+} defect centers can form then selves on the surface or within the lattice of TiO_2 [72]. The interaction between the defect sites (Ti^{3+}) and gold clusters plays a significant role in the photocatalytic activity [72]. The uniformly dispersed and small size of spheres of gold (ca. 23.3 nm) almost completely filled the surface defect of TiO_2 ($Ti^{3+} \sim 2\%$) which caused a reduction in the rate of recombination of electron-hole pairs. In the case of the highest size of rods (ca. 44 nm) and stars (ca.150 nm) the TiO_2 surface defect sites (Ti^{3+}) were not completely filled. The efficiency of phenol degradation under vis light for Au loaded on amorphous form of TiO_2 increased with the decrease the surface defect (Ti^{3+}). It was also observed, the increase of photoactivity with the increase of the carbon amount on the surface of amorphous form of TiO_2. According the literature, the photocatalysts containing more carbon species clearly showed a better activity [63,64]. Therefore, the highest amount of carbon in Au_NSPs_TiO_2 explained the photochemical reactivity under vis light. This could be a result of the tannic acid used as the main carbon source. The lowest content of carbon in Au nanorods (6.4 wt%) and nanostars (7.1 wt%) loaded on amorphous form of TiO_2 results a low photocatalytic efficiency. In this way, these samples had also lower activity compared to pristine of amorphous form of TiO_2 containing 9.8 wt% of carbon on surface.

In the case of anatase microspheres loaded with NSPs, NRs and NSTs calcinated at 400 °C before modification, the same tendency was observed. Since gold nanospheres have been attached on the surface of TiO_2 microspheres, the photocatalytic activity of Au-TiO_2 under visible light irradiation was higher than compared to nanorods and nanostars. One key factor in determining the photoactivity in these series was also the amount of surface defect (Ti^{3+}) and carbon on the surface photocatalysts. The active sample in series Au_NSPs_anatase had the highest content of carbon (25.4 wt%). The amount of defect site (Ti^{3+}) was lower (2.5%) which might be attributed to adsorption of small spheres on Ti^{3+} sites. The second parameter was effect of gold concentration on the activity. In this context it was prepared the five times higher concentration with different shape of gold. There was no radical changes in the photocatalytic activity with respect to series of lower gold concentration. It might be suggested that the photocatalytic activity depends on the size and shape obtained particle.

The different geometry of gold deposited on the rutile powders TIO-6, was also investigated. It was observed that all obtained samples Au-TIO-6 showed an efficient photocatalytic activity under Vis light compared to the pure TIO-6. The interesting thing was that the photoactivity of samples decreased in following order: NSPs > NRs > NSTs. The same tendency was observed for TiO_2 microspheres (anatase and pristine) modified by gold. Based on XPS analysis could be concluded that photocatalytic activity of two different matrix such as: rutile TIO-6 and anatas TiO_2 microspheres depends on the amount of gold on the surface. The increase of the amount of gold on the surface led to the increase of these samples activity. The contact between gold and titania varied for rutile TIO-6 and anatase TiO_2 microspheres as evidenced by the different gold content at the surface. The anatase of TiO_2 microspheres with surface porosity had an absolutely higher content of gold on the surface compared to rutile TiO_2. Nevertheless, the rutile phase was favorable for higher activity. This suggested that not only the shape and size but also the different matrix type could be an important point in the efficiency of photoactivity, what was also evidenced by Kowalska et al. [31,62].

Quite unlike is the situation for nanocomposites Au-NSPs, NRs and NSTs-TiO_2 calcined after modification of metal. These samples showed similar levels of visible light-induced activity, which could be related to spherical shape of gold nanoparticles, with the size range of 25–55 nm, formed at the surface of TiO_2 during thermal treatment. Thus, these results are consistent with the result obtained by the SEM/TEM analysis as well as the optical properties of Au-TiO_2. In the case of the smaller NSPs of gold (ca.25 nm) the higher level of activity and LSPR was observed at shorter wavelength. Moreover, the lower photoactivity was observed for the

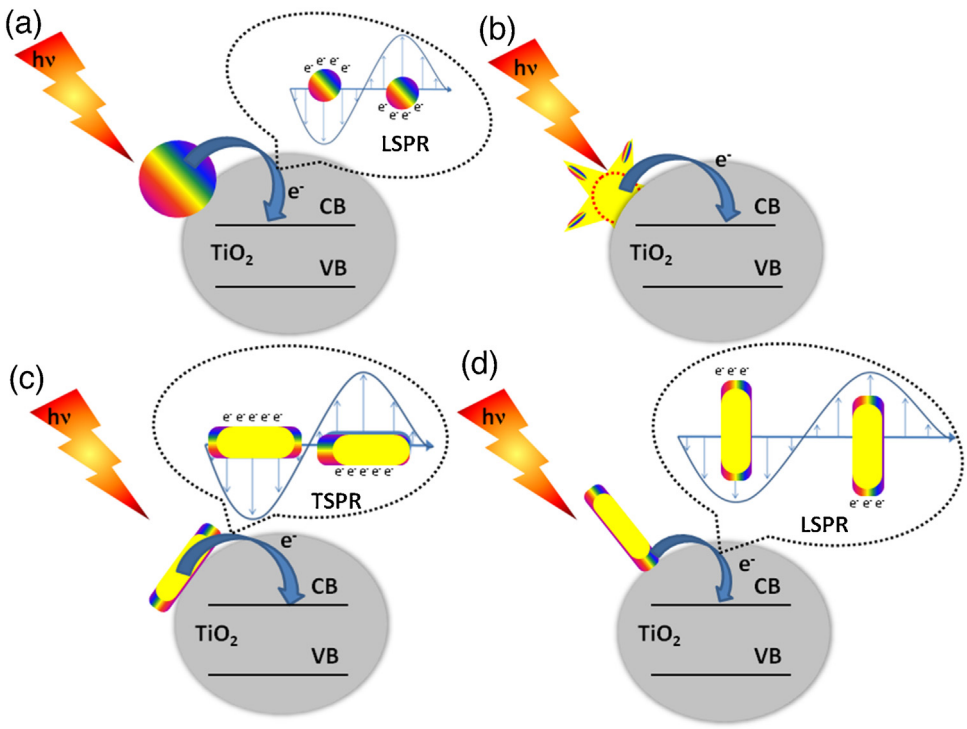

Fig. 9. The effect of gold nanoparticles shape on the mechanism of Au-TiO_2 excitation under visible light and interaction between TiO_2 matrix and gold nanospheres (a); gold nanostars (b); gold nanorods attached by elongated axis (c); and gold nanorods attached by narrower axis (d).

large NSPs with the size at about 55 nm and LSPR at longer wavelengths.

Generally, it was observed that photoactivity may be the result of two competing phenomena: (i) the samples photocatalytic efficiency is ascribed to the geometry of gold, and (ii) the Au-TiO_2 photocatalytic activity increases with the decrease of the particle size of gold.

The relative cluster sizes affect on the metal-titania binding and diffusion rates. Stronger metal–titania binding results in slower diffusion rates and smaller clusters with higher cluster densities [73]. Subramanian et al. [74] suggested that the greater shift in the Fermi level observed for smaller Au nanoparticle is reflected in the greater photocatalytic reduction efficiency. The apparent Fermi level as determined for Au-TiO_2 system was −250, −270 and−290 mV for 8, 5 and 3 nm Au-NPs, respectively. This shift of Fermi level to more negative potential is the result of a higher electron accumulation degree causing the composite system to be more reductive than the pristine TiO_2 system [75]. Nevertheless, the difference in the photocatalytic activity between these three different geometry of gold samples, could be related to different content of gold in the form of electropositive species ($Au^{\delta+}$). It can be observed that the electropositively charged Au species, characteristic for highly dispersed gold clusters, to be the most pronounced in NSTs and less contributed in NRs and NSPs. This tendency is observed in both, anatase and rutile supported samples. The more gold in the form of electropositive the more complex with Cl^- that may block the some active sites of TiO_2 which would have a negative influence on the photocatalytic activity.

Generally, for the gold nanoparticles the mechanism of plasmon enhanced photocatalysis is based on the local electric field enhancement associated with plasmonic nanoparticles. The plasmon enhancement was attributed to the strong electric fields produced by the surface plasmon resonance of Au. The collective oscillations of conduction electrons in metal nanoparticles resonate with the electromagnetic field of the incident light, which results in a considerable enhancement of the local electromagnetic fields. [76]. In this way the electrons were transfered from plasmonically excited Au nanoparticle to conduction band of titania. The mechanism for nanospheres of gold has an exactly the same way as in the case of Au nanoparticles as described above is shown in Fig. 9a. However, not all the Au geometries favor the recombination the same way. The nanostars loaded on the TiO_2 performed a lower visible activity and unimproved efficiency of interfacial charge transfer process. It would seem that the most “detrimental” recombination mechanism is the one described for the nanostars (Fig. 9b). The charge carriers trapping (e-/h+) is complicated by the center of nanostars. It is strictly related with the very low electromagnetic fields localized in middle of nanostars. The proposed mechanism induces electrons from the Au nanostars center with a very low electromagnetic field are transferred directly to the TiO_2 conduction band. This causes an increase in the recombination process rate of an electron-hole pairs which are associated with a reduced quantum yield of the reaction. Moreover, according to the SEM analysis stated that the nanostars deposited on the TiO_2 surface by “sinking” the long nanostars branches. Therefore, the inducted electron is transferred from the nanostars center without its long branches. The wide interface periphery between the nanostars core to spherical TiO_2 surface, was observed. For nanostars deposited on TiO_2 the LSPR was observed at 557 and 584 nm for Au-NSTs-TiO_2 of amorphous and Au-NSTs-TiO_2-un-amorphous. The position of this peaks responds for center of nanostars which have very low electromagnetic fields localized. Guerrero-Martínez et al. [55] stated that the very high electromagnetic fields were localized at each tip of the sharp long branches of nanostars. The specific frequency of these resonances varies as a function of the nanoparticle morphology (size and shape), and the dielectric properties of the surrounding medium, with deviations from the spherical symmetry led to LSPR red-shifts [55]. In the case of the nanorods, it is supposed that in the mechanism of NRs excitation under vis light the orientation of the NRs on the semiconductor surface is a very important point. In our case under the excitation of the transverse plasmon resonance of the nanorods array, electrons are transferred to the conduction

band of TiO_2 (Fig. 9c). It is believed that only longitudinal plasmon better promotes the direct transfers of charge between the two materials as shown in Fig. 9d. In this case the longitudinal plasmon is not directly involved in the mechanism of an electron transfer from the Au NRs to TiO_2. Based to the SEM analysis it was confirmed that the nanorods deposited on the TiO_2 surface by the transverse part of gold NRs. Therefore, the inducted electron is transferred from the transverse part to CB of titania. Liu et al. [33] stated that the large photocatalytic activity enhancement was induced by longitudinal plasma of Au NRs. The photocatalytic activity induced by longitudinal plasma of Au NRs could also be clarified by comparing with the photocatalytic activity induced and not only transversal but also longitudinal plasma of Au NRs. This may be due to the constraint of charge accumulation and mobility of the photoexcited electrons in Au NRs. They suggested that the nanorods of gold may lower the substrate adsorption and hinder the direct light absorption on the oxide surface and thus reduced the photogeneration of the charged species and the photoactivity [77]. Kowalska et al. [78] demonstrated that the field enhancement for NPs could indicate the higher photoactivity level. However, the higher ability of charge generation at the interface does not mean the higher photoactivity. Indeed, the plasmonic metals can be excited at the visible wavelengths *via* d-to-sp band transitions, recombining upon relaxation; once there is a pair of metals the relaxation is expected to be more efficient due to the larger available electronic states density [78].

In summary, our results clearly showed that the shape and also the size of the gold nanoparticles had a significant impact on the visible light induced photocatalytic activity of the Au-TiO_2 composites. Additionally, the matrix types of TiO_2 represented important point in the efficiency of photoactivity [75].

5. Conclusion

On the basis of these results it could be stated that the photocatalytic activity of Au-TiO_2 composites under visible light is affected by the geometry and size of gold nanoparticles immobilized at the surface of TiO_2. The best photocatalytic activity under visible light irradiation was observed for the amorphous form of TiO_2 sample modified by spherical particles of gold. The average rate of phenol decomposition was 1.9 $\mu mol\,dm^{-3}\,min^{-1}$ and was five and seven-times higher compared to nanorods and nanostars loaded on microspheres of TiO_2, respectively. The visible light activity decreased in following order: NSPs > NRs > NSTs. The difference of charge carriers (e−/h+) trapping for different geometry of gold nanoparticles, could be responsible for the observed photocatalytic activity. Moreover, the difference in the photocatalytic activity between these three different geometry of gold samples, could be related to (i) the different content of gold in the form of electropositive species ($Au^{\delta+}$), (ii) the amount of Ti^{3+} defect centers, (iii) the content of carbon on the surface. It can be observed that the electropositively charged Au species, characteristic for the highly dispersed gold clusters, to be the most pronounced in NSTs and less contributed in NRs and NSPs. Additionally, in these paper it was demonstrated, that the thermal treatment of Au-TiO_2 composites at 400 °C resulted in gold particles transformation from the others shapes into spheres and increased in size due to the gold nanoparticles melting, clusters mobility and Ostwald ripening. The microscopy analysis revealed a clear difference in gold particles size before and after calcination at 400 °C. The average size of NPs was definitely higher after the thermal treatment step and increased from 23 nm to about 35 nm. Generally, there could be two possibilities (i) the photocatalytic efficiency of samples was ascribed to the geometry of gold (*ii*) the photocatalytic activity of the Au-TiO_2 increases with the decrease of the particle size of gold.

Acknowledgments

The authors A.G., A.C. and A.Z. acknowledge funding from the National Science Centre, Poland (research grant: "Preparation and characteristics of novel three-dimensional semiconductor-based nanostructures using a template-free methods"; No.2011/03/B/ST5/03243) for work described here. The author G.M. M.J. and S.J. acknowledge funding from The National Centre for Research and Development, Poland (research grant: "Nanomaterials and their application to biomedicine", No. PBS1/A9/13/2012).

Appendix A. Supplementary data

Supplementary data associated with this article can be found, in the online version, at http://dx.doi.org/10.1016/j.apcatb.2016.05.013.

References

[1] S.T. Sivapalan, B.M. DeVetter, T.K. Yang, T. van Dijk, M.V. Schulmerich, P.S. Carney, R. Bhargava, C.J. Murphy, ACS Nano 7 (2013) 2099–2105.
[2] P.-P. Fang, X. Lu, H. Liu, Y. Tong, TrAC Trends Anal. Chem. 66 (2015) 103–117.
[3] G. Bi, W. Xiong, L. Wang, K. Ueno, H. Misawa, J.-r. Qiu, Opt. Commun. 285 (2012) 2472–2477.
[4] A. Ayati, A. Ahmadpour, F.F. Bamoharram, B. Tanhaei, M. Mänttäri, M. Sillanpää, Chemosphere 107 (2014) 163–174.
[5] B. Dai, X. Li, J. Zhang, F. Yu, M. Zhu, Chem. Eng. Sci. 135 (2015) 472–478.
[6] W. Wang, F. Wang, Y. Kang, A. Wang, Chem. Eng. J. 237 (2014) 336–343.
[7] S.S. Rayalu, D. Jose, M.V. Joshi, P.A. Mangrulkar, K. Shrestha, K. Klabunde, Appl. Catal. B: Environ. 142–143 (2013) 684–693.
[8] S. Bouhadoun, C. Guillard, F. Dapozze, S. Singh, D. Amans, J. Bouclé, N. Herlin-Boime, Appl. Catal. B: Environ. 174–175 (2015) 367–375.
[9] Z.-D. Gao, Y.-Y. Han, Y.-C. Li, M. Yang, Y.-Y. Song, Electrochim. Acta 125 (2014) 530–535.
[10] P. Kannan, S.A. John, Electrochim. Acta 56 (2011) 7029–7037.
[11] J. Zhu, Z. Xu, B. Lu, Nano Energy 7 (2014) 114–123.
[12] X. Wu, A. Centeno, X. Zhang, D. Darvill, M.P. Ryan, D.J. Riley, N.M. Alford, F. Xie, Sol. Energy Mater. Sol. Cells 138 (2015) 80–85.
[13] M.-C. Daniel, D. Astruc, Chem. Rev. 104 (2004) 293–346.
[14] L. DuLiang, L. Xian, J.-X. Feng, J. Nanopart. Res. 13 (2011) 921–930.
[15] E.M. Smoak, A.D. Carlo, C.C. Fowles, I.A. Banerjee, Nanotechnology 21 (2010).
[16] N.U. Islam, K. Jalil, M. Shahid, N. Muhammad, A. Rauf, Arabian J. Chem. (2016) (in press).
[17] P.K. Jain, K.S. Lee, I.H. El-Sayed, M.A. El-Sayed, J. Phys. Chem. B 110 (2006) 7238–7248.
[18] P. Yan, N. Zhao, H. Hu, X. Lin, F. Liu, F.-J. Xu, Acta Biomater. 10 (2014) 3786–3794.
[19] S. Zeng, K.-T. Yong, I. Roy, X.-Q. Dinh, X. Yu, F. Luan, Plasmonics 6 (2011) 491–506.
[20] D. Seo, J.C. Park, H. Song, J. Am. Chem. Soc. 128 (2006) 14863–14870.
[21] S. Eustis, M.A. El-Sayed, Chem. Soc. Rev. 35 (2006) 209–217.
[22] M.R. Dewi, G. Laufersky, T. Nann, RSC Adv. 4 (2014) 34217–34220.
[23] D. Liu, C. Li, F. Zhou, T. Zhang, H. Zhang, X. Li, G. Duan, W. Cai, Y. Li, Sci. Rep. 5 (2015).
[24] S. Link, C. Burda, B. Nikoobakht, M.A. El-Sayed, J. Phys. Chem. B 104 (2000) 6152–6163.
[25] C. Wang, Y. Hu, C.M. Lieber, S. Sun, J. Am. Chem. Soc. 130 (2008) 8902–8903.
[26] Yanxiao Li, Zhanfang Ma, Nanotechnology 24 (2013) 275605.
[27] E. Hao, R.C. Bailey, G.C. Schatz, J.T. Hupp, S. Li, Nano Lett. 4 (2004) 327–330.
[28] L. Vigderman, E.R. Zubarev, Starfruit-shaped gold nanorods and nanowires: synthesis and SERS characterization, Langmuir 28 (2012) 9034–9040.
[29] A. Horneber, K. Braun, J. Rogalski, P. Leiderer, A.J. Meixner, D. Zhang, Phys. Chem. Chem. Phys. (2015).
[30] H. Chen, L. Shao, Q. Li, J. Wang, Chem. Soc. Rev. 42 (2013) 2679–2724.
[31] E. Kowalska, O.O.P. Mahaney, R. Abe, B. Ohtani, Phys. Chem. Chem. Phys. 12 (2010) 2344–2355.
[32] S.R. Ewa Kowalska, Bunsho Ohtani, Plasmonic titania photocatalysts active under UV and visible-light irradiation: influence of gold amount, size, and shape, J. Nanotechnol. 2012 (2012), 11 page.
[33] L. Liu, S. Ouyang, J. Ye, Angew. Chem. Int. Ed. 52 (2013) 6689–6693.
[34] Y. Nishijima, K. Ueno, Y. Yokota, K. Murakoshi, H. Misawa, J. Phys. Chem. Lett. 1 (2010) 2031–2036.
[35] I. Tanabe, T. Ryoki, Y. Ozaki, RSC Adv. 5 (2015) 13648–13652.
[36] R. Kaur, B. Pal, J. Mol. Catal. A: Chem. 355 (2012) 39–43.
[37] Z. Réka Tóth, Z. Pap, Virginia Danciu, Lucian Baia, G. Kovács, Differently shaped Au nanoparticles: a case study on the enhancement of the photocatalytic activity of commercial TiO_2, Materials (2015) 162–180.
[38] Y.-C. Pu, G. Wang, K.-D. Chang, Y. Ling, Y.-K. Lin, B.C. Fitzmorris, C.-M. Liu, X. Lu, Y. Tong, J.Z. Zhang, Y.-J. Hsu, Y. Li, Nano Lett. 13 (2013) 3817–3823.

[39] Y. Zheng, J. Cai, K. Lv, J. Sun, H. Ye, M. Li, Appl. Catal. B: Environ. 147 (2014) 789–795.
[40] C. Wang, H. Liu, Y. Liu, G.a. He, C. Jiang, Appl. Surf. Sci. 319 (2014) 2–7.
[41] R. Wang, X. Cai, F. Shen, Ceram. Int. 39 (2013) 9465–9470.
[42] Z. Zheng, B. Huang, X. Qin, X. Zhang, Y. Dai, Chem. Eur. J. 16 (2010) 11266–11270.
[43] C. Guo, M. Ge, L. Liu, G. Gao, Y. Feng, Y. Wang, Environ. Sci. Technol. 44 (2010) 419–425.
[44] S. Aswathy Aromal, D. Philip, Phys. E: Low Dimens. Syst. Nanostruct. 44 (2012) 1692–1696.
[45] D. Kozanoglu, D.H. Apaydin, A. Cirpan, E.N. Esenturk, Org. Electron. 14 (2013) 1720–1727.
[46] B. Nikoobakht, M.A. El-Sayed, Chem. Mater. 15 (2003) 1957–1962.
[47] M. Chen, D.W. Goodman, Chem. Soc. Rev. 37 (2008) 1860–1870.
[48] Y. Wen, B. Liu, W. Zeng, Y. Wang, Nanoscale 5 (2013) 9739–9746.
[49] T. Akita, P. Lu, S. Ichikawa, K. Tanaka, M. Haruta, Surf. Interface Anal. 31 (2001) 73–78.
[50] V. Sharma, K. Park, M. Srinivasarao, Mater. Sci. Eng.: R: Rep. 65 (2009) 1–38.
[51] F. Kim, J.H. Song, P. Yang, J. Am. Chem. Soc. 124 (2002) 14316–14317.
[52] L.T. Lanh, T.T. Hoa, N.D. Cuong, D.Q. Khieu, D.T. Quang, N. Van Duy, N.D. Hoa, N. Van Hieu, J. Alloys Compd. 635 (2015) 265–271.
[53] X. Ma, M.-C. Wang, J. Feng, X. Zhao, J. Alloys Compd. 637 (2015) 36–43.
[54] X. Zhong, Y.-Q. Chai, R. Yuan, Talanta 128 (2014) 9–14.
[55] A. Guerrero-Martínez, S. Barbosa, I. Pastoriza-Santos, L.M. Liz-Marzán, Curr. Opin. Colloid Interface Sci. 16 (2011) 118–127.
[56] E.S. Kooij, W. Ahmed, C. Hellenthal, H.J.W. Zandvliet, B. Poelsema, Colloids Surf. A 413 (2012) 231–238.
[57] C. Nehl, H. Liao, J. Hafner, Synthesis and optical properties of star-shaped gold nanoparticles, Nano Lett. (2006).
[58] P.S. Kumar, I. Pastoriza-Santos, B. Rodríguez-González, F.J.G.d. Abajo, L.M. Liz-Marzán, Nanotechnology 19 (2008).
[59] Y.X. Li, J. Ma, Z.F. Ma, Electrochim. Acta 108 (2013) 435–440.
[60] P. Jain, X. Huang, I. El-Sayed, M. El-Sayed, Plasmonics 2 (2007) 107–118.
[61] A.R. Senoudi, S.M. Chabane Sari, I.F. Hakem, Int. J. Anal. Chem. 2014 (2014).
[62] E. Kowalska, R. Abe, B. Ohtani, Chem. Commun. (2009) 241–243.
[63] A. Cybula, J.B. Priebe, M.-M. Pohl, J.W. Sobczak, M. Schneider, A. Zielińska-Jurek, A. Brückner, A. Zaleska, Appl. Catal. B: Environ. 152–153 (2014) 202–211.
[64] P. Górska, A. Zaleska, E. Kowalska, T. Klimczuk, J.W. Sobczak, E. Skwarek, W. Janusz, J. Hupka, Appl. Catal. B: Environ. 84 (2008) 440–447.
[65] B. Tryba, J. Orlikowski, R.J. Wróbel, J. Przepiórski, A.W. Morawski, J. Mater. Eng. Perform. 24 (2015) 1243–1252.
[66] H. Jensen, A. Soloviev, Z. Li, E.G. Sogaard, Appl. Surf. Sci. 246 (2005) 239–249.
[67] J. Yu, X. Zhao, Q. Zhao, Thin Solid Films 379 (2000) 7–14.
[68] A. Rjeb, S. Letarte, L. Tajounte, M.C. El Idrissi, A. Adnot, D. Roy, Y. Claire, J. Kaloustian, J. Electron Spectrosc. Relat. Phenom. 107 (2000) 221–230.
[69] A. Zielińska-Jurek, E. Kowalska, J.W. Sobczak, W. Lisowski, B. Ohtani, A. Zaleska, Appl. Catal. B: Environ. 101 (2011) 504–514.
[70] J.A. Moma, M.S. Scurrell, W.A. Jordaan, Top. Catal. 44 (2007) 167–172.
[71] S. Shukla, S. Seal, Nanostruct. Mater. 11 (1999) 1181–1193.
[72] T. Bennett, R.H. Adnan, J.F. Alvino, R. Kler, V.B. Golovko, G.F. Metha, G.G. Andersson, J. Phys. Chem. C 119 (2015) 11171–11177.
[73] R.P. Galhenage, H. Yan, S.A. Tenney, N. Park, G. Henkelman, P. Albrecht, D.R. Mullins, D.A. Chen, J. Phys. Chem. C 117 (2013) 7191–7201.
[74] V. Subramanian, E.E. Wolf, P.V. Kamat, J. Am. Chem. Soc. 126 (2004) 4943–4950.
[75] A. Gołąbiewska, W. Lisowski, M. Jarek, G. Nowaczyk, A. Zielińska-Jurek, A. Zaleska, Appl. Surf. Sci. 317 (2014) 1131–1142.
[76] A. Bumajdad, M. Madkour, Phys. Chem. Chem. Phys. 16 (2014) 7146–7158.
[77] R. Kaur, B. Pal, Mater. Res. Bull. 62 (2015) 11–18.
[78] E. Kowalska, M. Janczarek, L. Rosa, S. Juodkazis, B. Ohtani, Catal. Today 230 (2014) 131–137.